Supporting Information

Through-space hopping transport in an iodine-doped perylene-based Metal-Organic Framework

Gonçalo Valente,[a] María Esteve-Rochina,[b] Ana Paracana,[c] Antonio Rodríguez-Diéguez,[d] Duane Choquesillo-Lazarte,[e] Enrique Ortí,[b] Joaquín Calbo,*[b] Marina Ilkaeva,[a] Luís Mafra,[a] Miguel A. Hernández-Rodríguez,[c] João Rocha,[a] Helena Alves[b] and Manuel Souto*[a]

Contents

1. General methods and materials

All reagents and solvents were of high purity grade and were purchased from Sigma-Aldrich Co., and TCI. ^{1}H liquid NMR spectra were recorded on a Bruker AVANCE 300 spectrometer (300 MHz). Dimethylsulfoxide-d_6 (DMSO-d_6) was used as solvent. Tetramethylsilane was used as the internal reference. Chemical shifts (δ) are quoted in ppm and the coupling constants (J) in Hz. Infrared spectra were recorded on an ATR FT-IR GALAXY SERIES FT-IR 7000 (Mattson Instruments) spectrometer in the 4000-400 cm^{-1} range using powdered samples. Raman spectra were recorded on a RFS 100/S (Bruker) spectrometer equipped with Nd:YAG laser (1064 nm) in the 4000-100 cm^{-1} range. Thermogravimetric analysis (TGA) was carried out with a Shimadzu TGA 50 equipment in the 25-600 ºC range with a 5 ºC/min scan rate and a N_2 flow of 20 $mL \cdot min^{-1}$. Powder X-ray diffraction patterns were recorded on an Empyrean PANalytical diffractometer (Cu $K\alpha_{1,2}$ X-radiation, λ_1 = 1.540598 Å; λ_2 = 1.544426 Å), equipped with an PIXcel 1D detector and a flat-plate sample holder in a Bragg-Brentano para-focusing optics configuration (45 kV, 40 mA).

2. Synthesis of H_4PTCA ligand

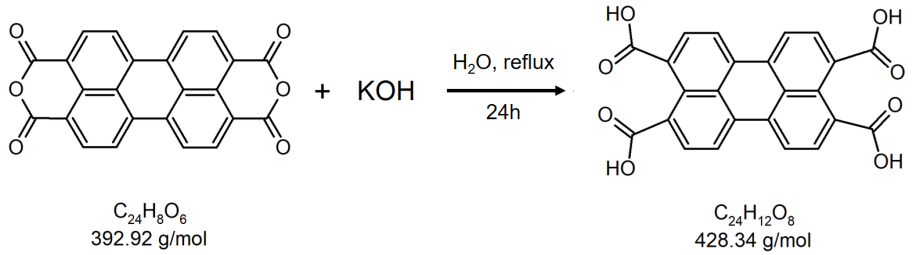

Scheme S1. Synthesis of 3,4,9,10-Perylenetetracarboxylic acid (H_4PTCA).

The ligand 3,4,9,10-perylenetetracarboxylic acid (H_4PTCA) was synthesized by reacting 3,4,9,10-perylenetetracaboxylicdianhydride (PTCDA) (500 mg, 1,27 mmol) and potassium hydroxide (500 mg, 9 mmol) in 50 mL of distilled water with vigorous stirring under reflux overnight. The resulting green solution was acidified with 1 M HCl (5 mL) yielding a red precipitate, which was filtered out and washed with water under reduced pressure. The resulting red powder was dried at 120 ºC giving 546 mg (97 %) of H_4PTCA. IR (cm^{-1}): 3000 (broad, OH), 1690 (s, C=O), 1590, 1516, 1435, 1394, 1370, 1274, 1217, 1190, 1025, 938, 848, 804, 754, 729, 638, 599, 569, 506. ^{1}H-NMR (300 MHz, DMSO-d_6): (ppm) 13.05 (s, 4H, COOH), 8.58 (d, 4H, Ar-H, J = 8.1 Hz), 8.01 (d, 4H, Ar-H, J = 7.9 Hz).

3. Synthesis of Per-MOF

Per-MOF crystals were obtained as previously reported:[1] 0.008 g of 3,4,9,10-perylenetetracarboxylic acid (0.1 mmol) were added to 5 mL of H_2O. The resulting solution was sonicated for 20 minutes, and then an aqueous solution (5 ml) containing KOH (0.1 mmol) was added. The reaction mixture was heated with IR light for 24 h. Orange prismatic crystals were obtained (yield = 63% based on K^+ ion).

4. Characterization of Per-MOF

4.1. IR spectroscopy

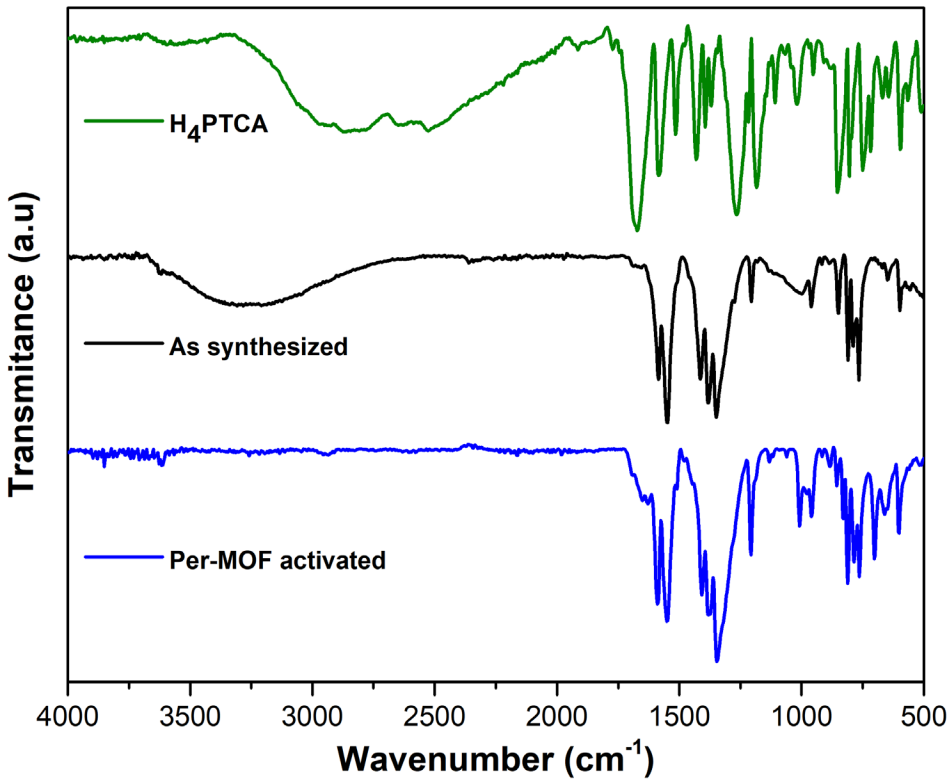

Fig. S1. FT-IR spectra of **H_4PTCA** ligand and as-synthesized and activated **Per-MOF**.

4.2. Crystal structure

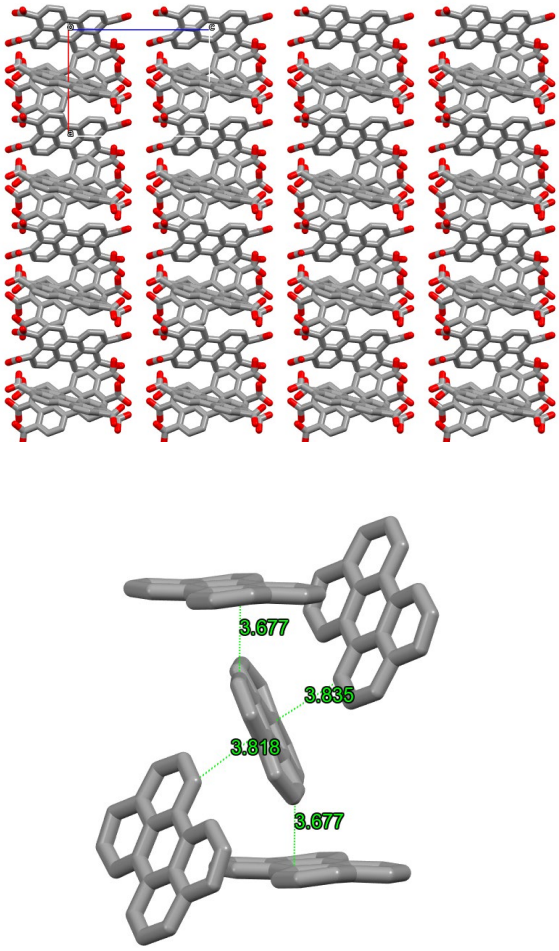

Fig. S2. Schematic representation of the herringbone arrangement of the perylene-based linkers along the *a*-axis showing the shortest C···C distances between neighbouring perylenes. Colour code: C (grey), O (red), K (purple). For simplicity, potassium and hydrogens are omitted.

Table S1. Porosity of **Per-MOF** as estimated from Olex2 CalcVoid/CalcSolv analysis with a 0.1 Å resolution.[2]

Radius largest spherical void	Structure volume	Cell volume	Penetration sphere radius	Solvent accessible
3.0 Å	1282 Å^3 (71%)	1799 Å^3	1.5 Å	317 Å^3 (18%)

4.3. Thermogravimetric analysis (TGA)

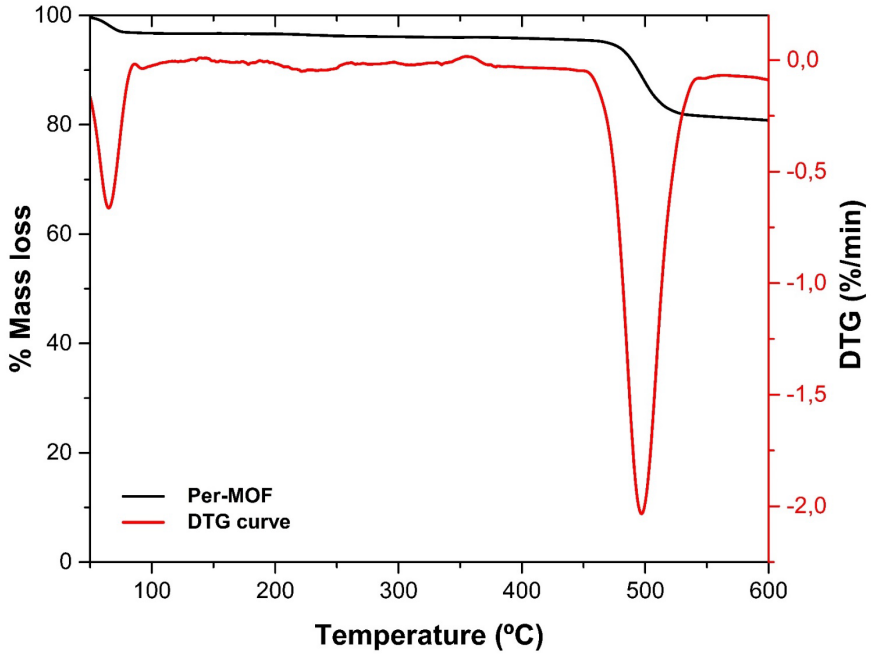

Fig. S3. Thermogravimetric analysis (TGA) profile of activated **Per-MOF** at a heating rate of 5 ºC min^{-1} under a constant stream of N_2 (black) and DTG curve (red).

4.4. Gas adsorption/desorption isotherms

A Microtrac Belsorp MAX II HP was used to obtain adsorption-desorption isotherms of N_2 at 77 K and CO_2 at 273 K. Before the experiment, the samples were outgassed under vacuum at 120 °C for 12 hours. The BET surface area (from the N_2 isotherm) was calculated to be 15 m^2 g^{-1} with a total pore volume of 0.08 cm^3 g^{-1}. The micropore volume ($V_{micro}DR$) was calculated to be 0.04 cm^3 g^{-1} using the Dubinin-Radushkevich method.

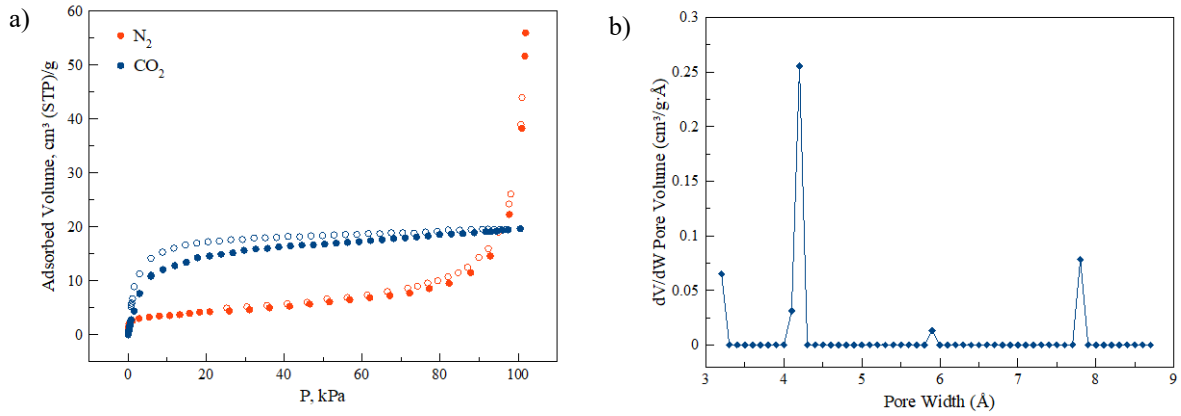

Fig. S4. a) N_2 (red) and CO_2 (blue) volumetric adsorption-desorption isotherms of **Per-MOF** measured at 77 and 273 K, respectively. Filled and open symbols represent the adsorption and the desorption branches, respectively. b) Pore size distribution for **Per-MOF** calculated by Grand Canonical Monte Carlo (GCMC) approach using a carbon slit-shaped pore model.

4.5. Cyclic voltammetry (CV)

Electrode preparation: The powdered materials (2mg) were mixed in 2 mL of Nafion and ethanol (1:3). 100 µL were deposited on a 3 mm diameter glassy carbon disc working electrode, which was previously polished with 0.3, 0.1 and 0.05 µm alumina powders. Afterwards, the solvent was evaporated at room temperature.

Equipment: The electrochemical experiments were performed on an Autolab electrochemical workstation (PGSTAT302N with FRA32M Module) connected to a personal computer that uses Nova 2.1 electrochemical software. A typical three-electrode experimental cell equipped with a platinum wire as the counter electrode, and a silver wire as the pseudoreference electrode was used for the electrochemical characterization of the working electrodes. The electrochemical properties were studied measuring CV under inert (N_2) atmosphere at different scan rates in previously N_2-purged 0.1 M $TBAPF_6/CH_3CN$ solutions. Ferrocene was added as an internal standard upon completion of each experiment. All potentials are reported in V versus Ag/AgCl.

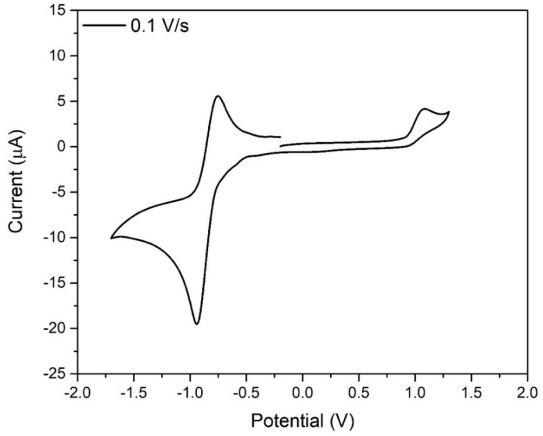

Fig. S5. Cyclic voltammetry of the **H_4PTC** ligand in DMF using $TBAPF_6$ 0.1 M as electrolyte at 0.1 V s^{-1} scan rate. Platinum wire was used as the counter electrode and silver wire as the pseudoreference electrode. Ferrocene was added as internal standard. All potentials are reported versus Ag/AgCl.

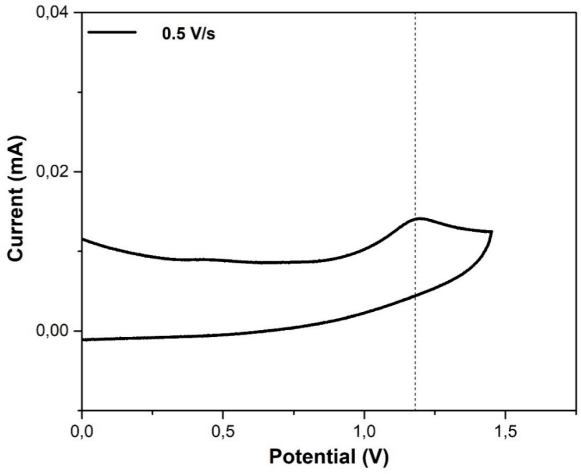

Fig. S6. Zoom into the solid-state cyclic voltammetry (CV) of **Per-MOF** in CH_3CN using $TBAPF_6$ 0.1 M as electrolyte at 0.5 V/s scan rate in the 0-2 V region. Platinum wire was used as the counter electrode and silver wire as the pseudoreference electrode. Ferrocene was added as internal standard. All potentials are reported versus Ag/AgCl.

5. Iodine doping and characterization of I_2@Per-MOF

Procedure: 50 mg of activated crystals (heated at 200 ºC for 2h) of **Per-MOF** were immersed in 8 mL of a saturated solution of iodine in cyclohexane (0.1 M) at room temperature for 24 hours. To ensure homogeneous doping of the framework, the material was stirred in the solution for 2 hours. Then, the crystals were washed with cyclohexane and dried at room temperature. Elemental analysis of $C_{72}H_{24}K_8O_{24}I_2$ (**I_2@Per-MOF**), calcd: I 12.72; K 23.51 found: I 11.92 K 22.62.

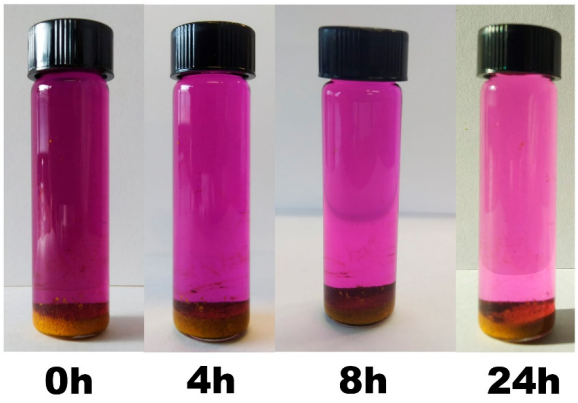

Fig. S7. I_2 doping process of crystals of Per-MOF soaked in 8 mL solution of iodine (0.1 M) in cyclohexane at room temperature.

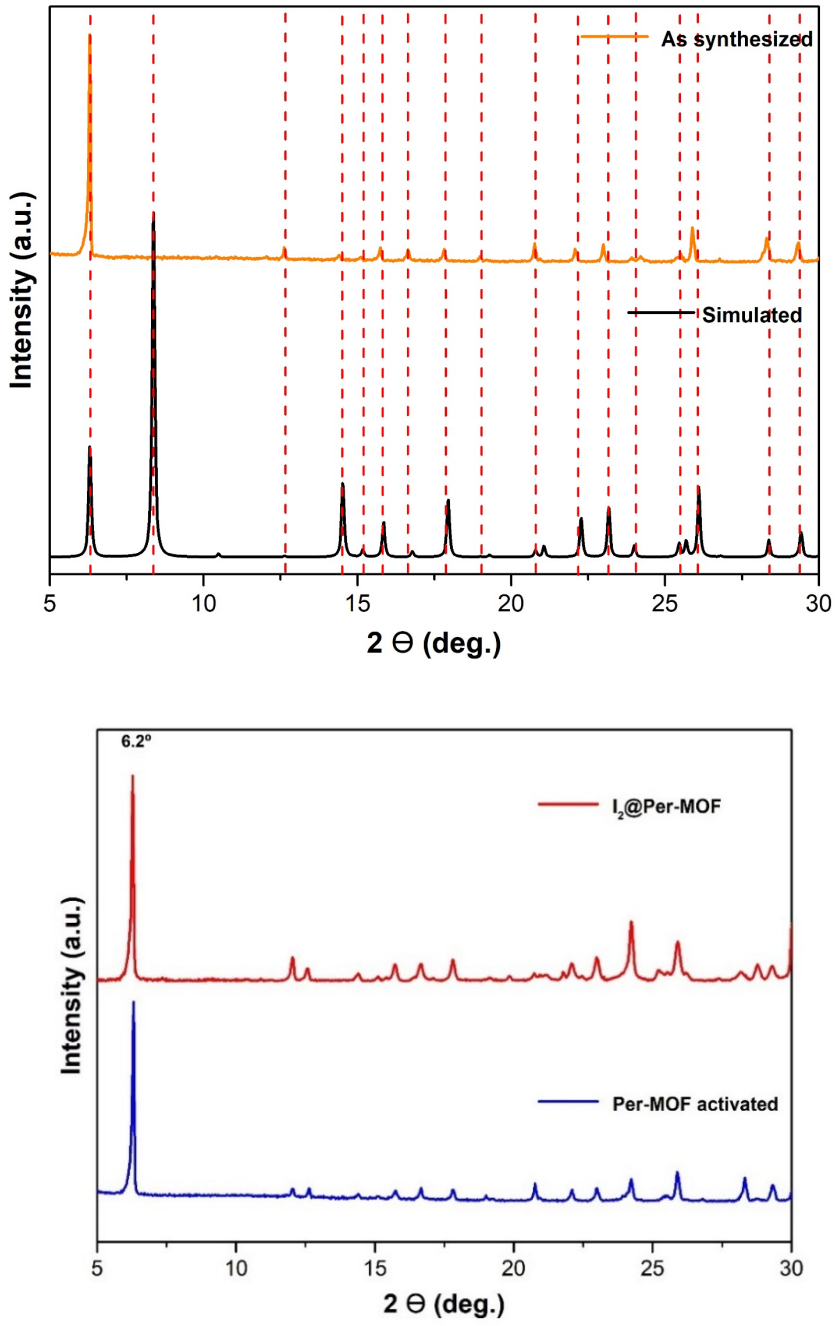

Fig. S8. Powder X-ray diffraction patterns of simulated, as-synthesized, activated **Per-MOF** and iodine-doped **I_2@Per-MOF**.

5.1. Scanning Electron Microscopy (SEM)

SEM images were acquired on a Hitachi S4100 field emission gun tungsten filament instrument working at 25 kV and on a high-resolution Hitachi SU-70 working at 4 kV. Samples were prepared by deposition on aluminium sample holders followed by carbon coating using an Emitech K950X carbon evaporator. EDS (Energy Dispersive X-ray Spectroscopy) data and SEM mapping images were recorded using the same microscope, Hitachi SU-70, working at 15 kV and using a Bruker Quantax 400 or a Sprit 1.9 EDS microanalysis system

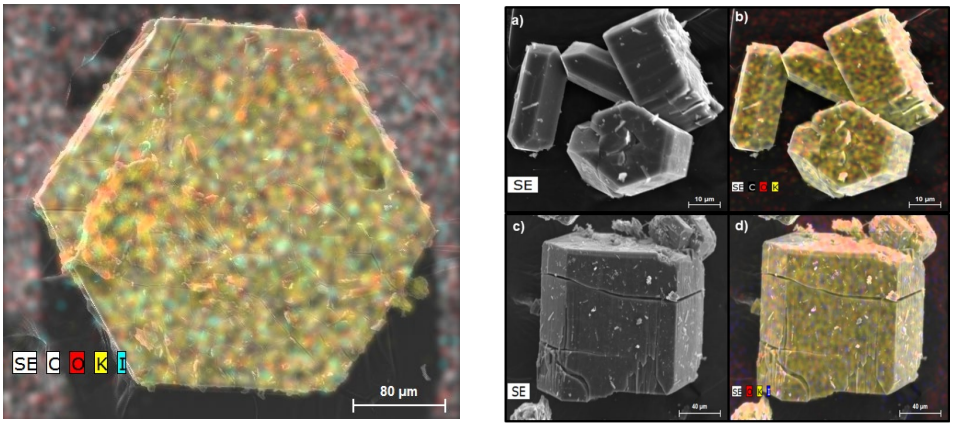

Fig. S9. SEM images and energy dispersive X-ray spectroscopy (EDS) of **Per-MOF** (a and b) and **I_2@Per-MOF** (c and d) crystals.

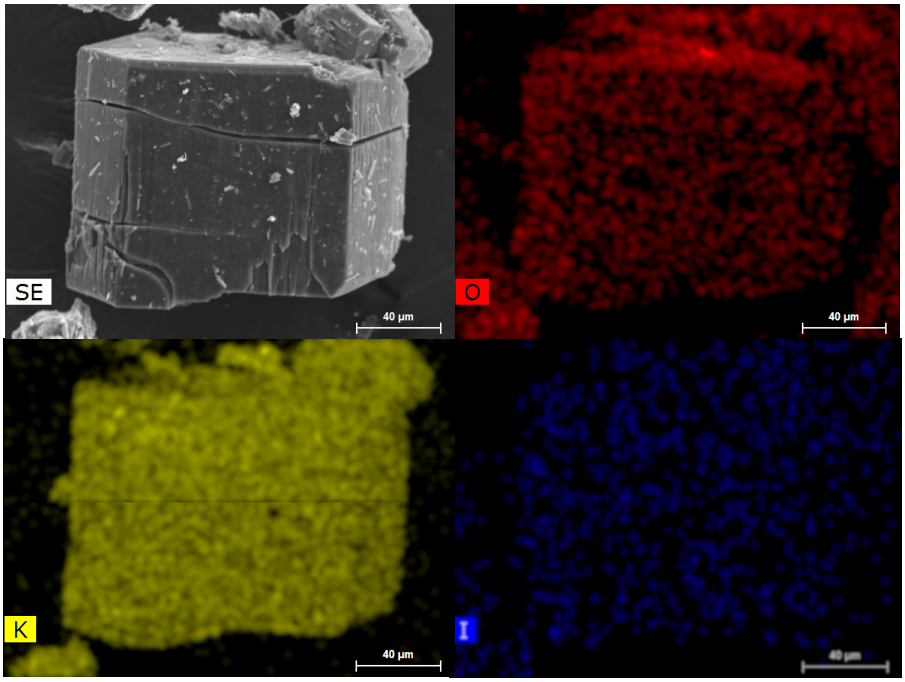

Fig. S10. SEM images and energy dispersive X-ray spectroscopy (EDS) of **I_2@Per-MOF**.

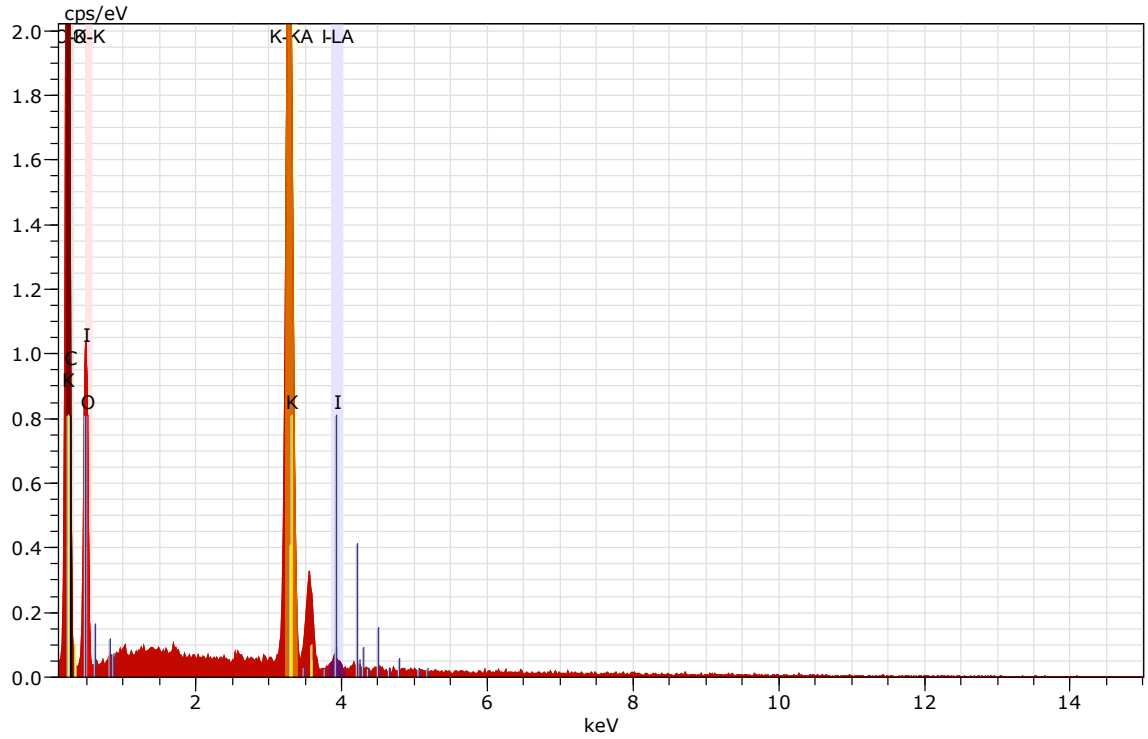

Fig. S11. EDS analysis of iodine-doped **Per-MOF** confirms the presence of all the elements (C, O, K, I).

5.2. IR and Raman spectroscopy

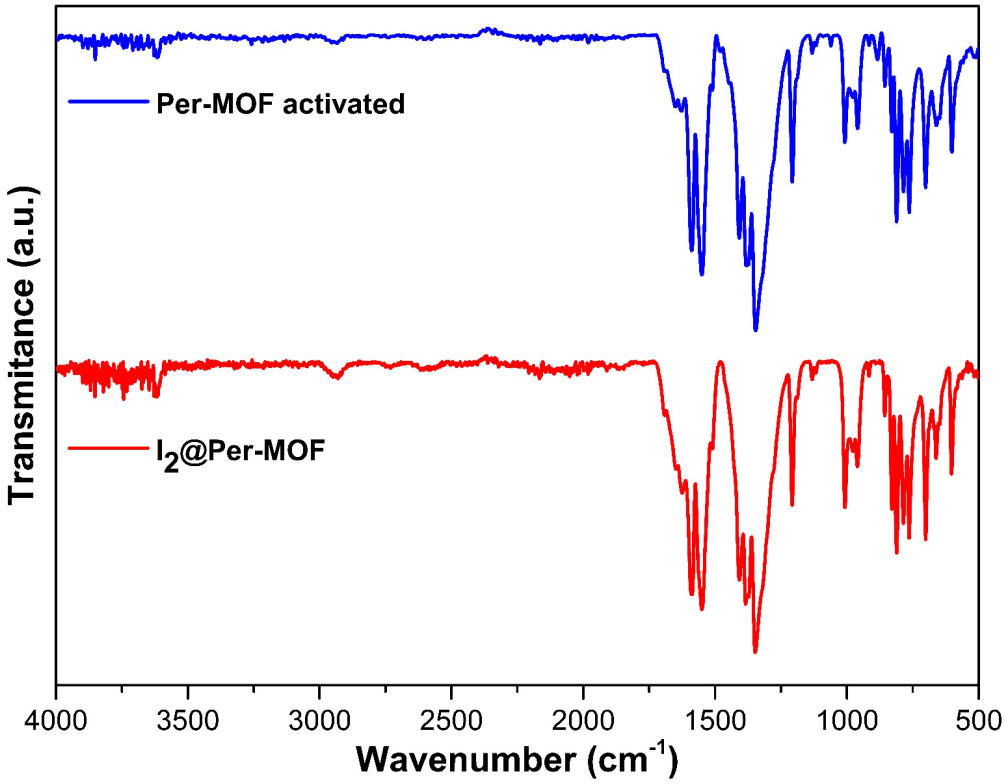

Fig. S12. FT-IR spectra of activated **Per-MOF** and **I_2@Per-MOF**.

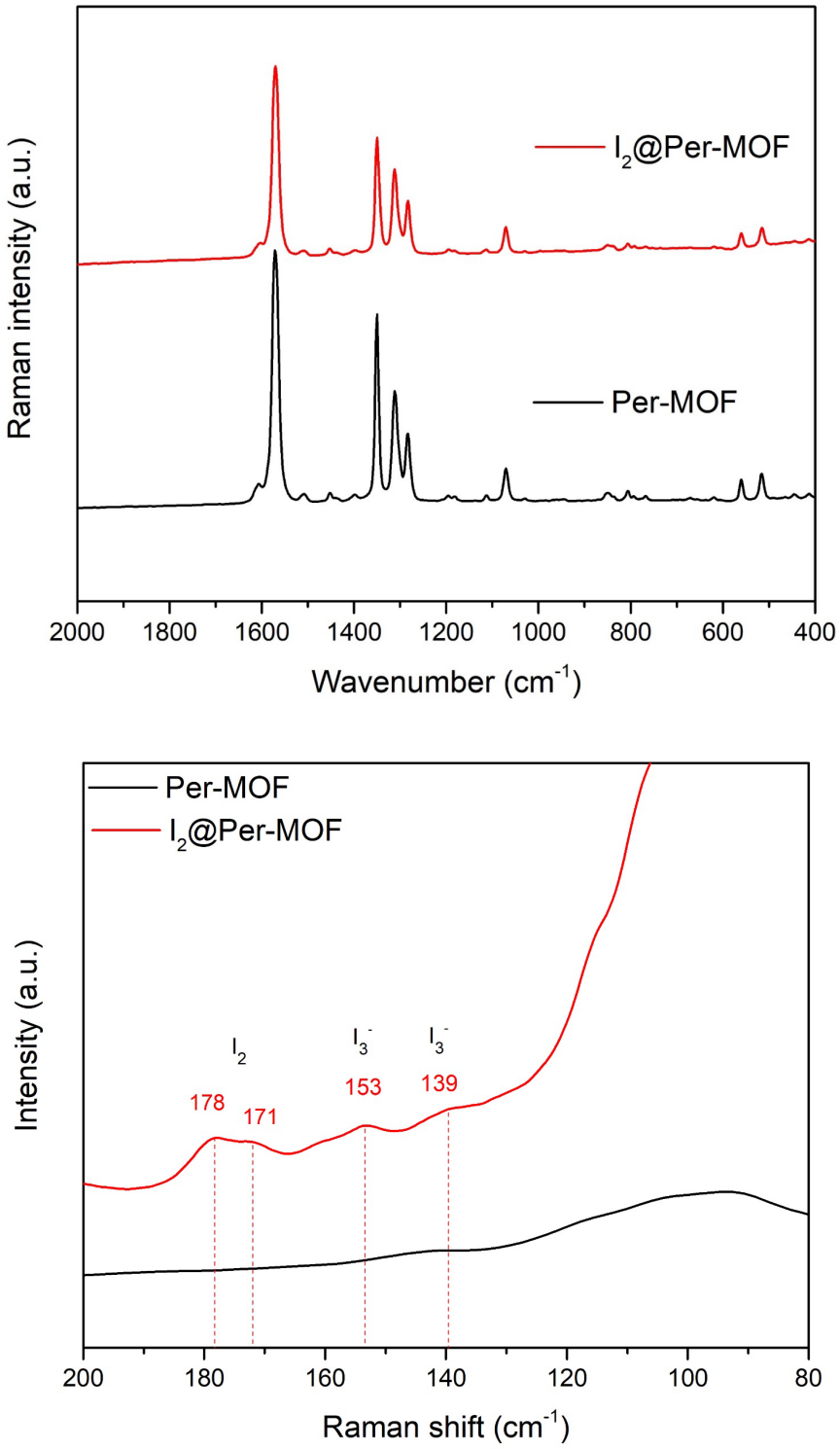

Fig. 13. Raman spectra (λ = 1064 nm) of **Per-MOF** and **I_2@Per-MOF** in the 2000-400 and 200-100 cm^{-1} regions.

5.3. Electron Paramagnetic Resonance (EPR) spectroscopy

EPR measurements of **Per-MOF** and **I_2@Per-MOF** crystals were carried out at room temperature on a Bruker ESP- 300E spectrometer operating in the X band 9.861 GHz and with a field modulation of 2 GHz.

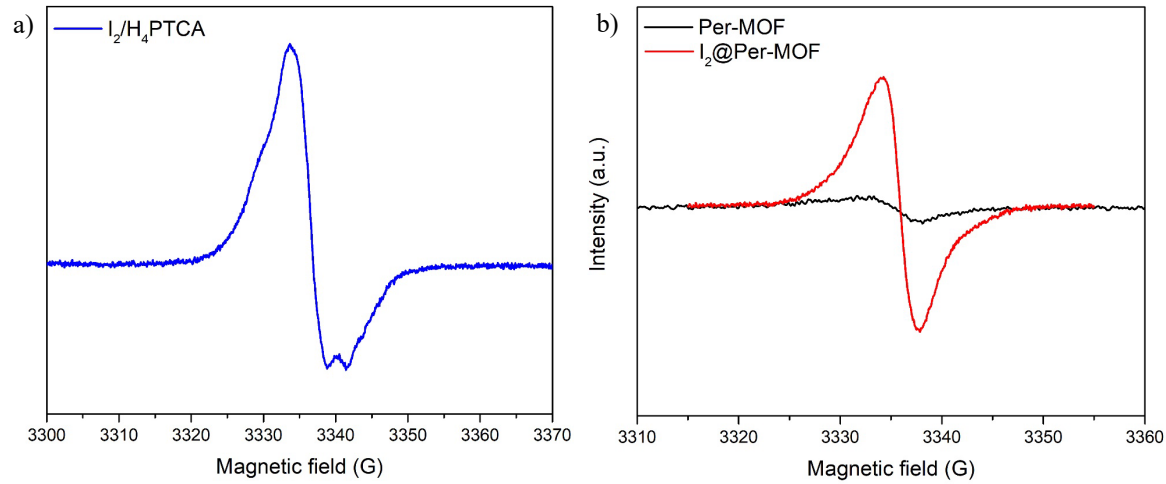

Fig. S14. EPR spectra of a) H_4PTCA ligand oxidized with iodine (used as reference); and b) **Per-MOF** and **I_2@Per-MOF** crystals (10 mg) at room temperature.

5.4. TGA of I_2@Per-MOF

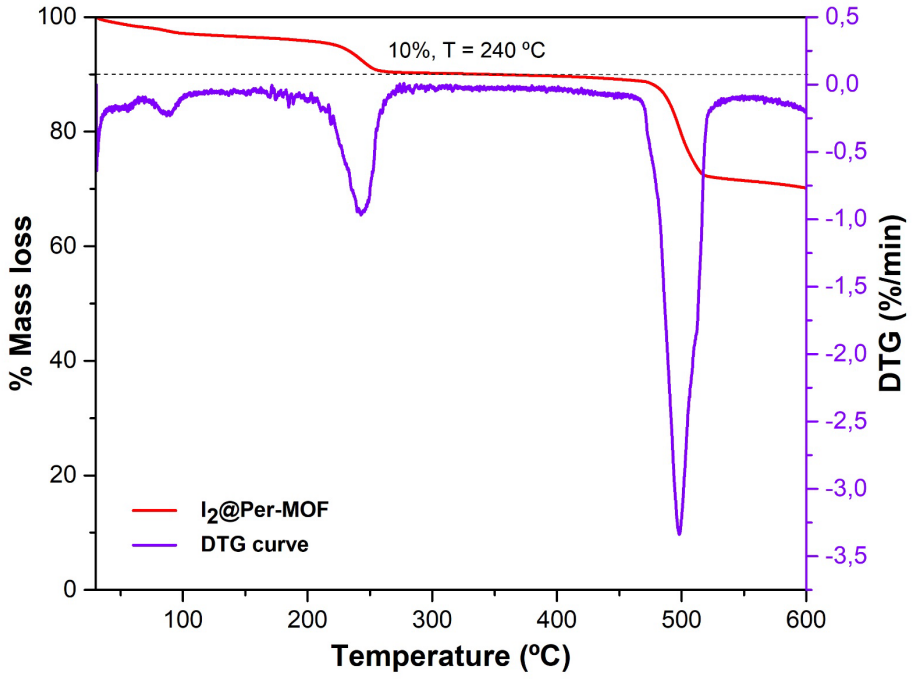

Fig. S15. Thermogravimetric analysis (TGA) profile of **I_2@Per-MOF** at a heating rate of 5 ºC min under a constant stream of N_2 (red) and DTG curve (purple). The mass loss of ca. 10% corresponds to one molecule of I_2 per three perylene ligands.

5.5. Optical measurements

UV/visible absorption and diffuse reflectance: The UV/visible absorption and diffuse reflectance spectra of the samples were measured using a Lambda 950 dual-beam spectrometer (PerkinElmer). The diffuse reflectance spectra are reported as the Kubelka-Munk transform, where $F(R) = (1-R)^2/2R$. The Kubelka–Munk function transformed spectra were then normalized with respect to F(R) at 400 nm. *Photoluminescence spectroscopy*: The emission and excitation spectra were recorded on a modular double grating excitation spectrofluorimeter with a TRIAX 320 emission monochromator (Fluorolog-3, Horiba Scientific) coupled to a near infrared R928 Hamamatsu photomultiplier, using the front face acquisition mode. The excitation source was a 450 W Xe arc lamp. Both recorded emission and excitation spectra were corrected with the spectrofluorimeter optical spectral response and the spectral distribution of the lamp intensity using a photodiode reference detector, respectively. Absolute photoluminescence quantum yield (PLQY) of **Per-MOF** and **I_2@Per-MOF** were measured with a quantum yield measurement system Quantaurus-QY (C13534, Hamamatsu), equipped with a 150 W Xenon lamp coupled to a monochromator for wavelength discrimination, an integrating sphere as sample chamber and two multi-channel analyzers for signal detection in the visible and in the NIR spectral ranges. The excitation wavelength was 368 nm using the Xenon lamp. All measurements were performed in quartz holders in which the pressed pellet shaped samples were placed. As a reference sample, the empty quartz holder sample was used. PLQY was calculated by the quotient between the emitted and absorbed photons by the samples. The equipment's software computes the PLQY using the user-defined wavelength integration ranges for excitation and emission. According to the manufacturer, each measurement presents a relative systemic error of 10 %.

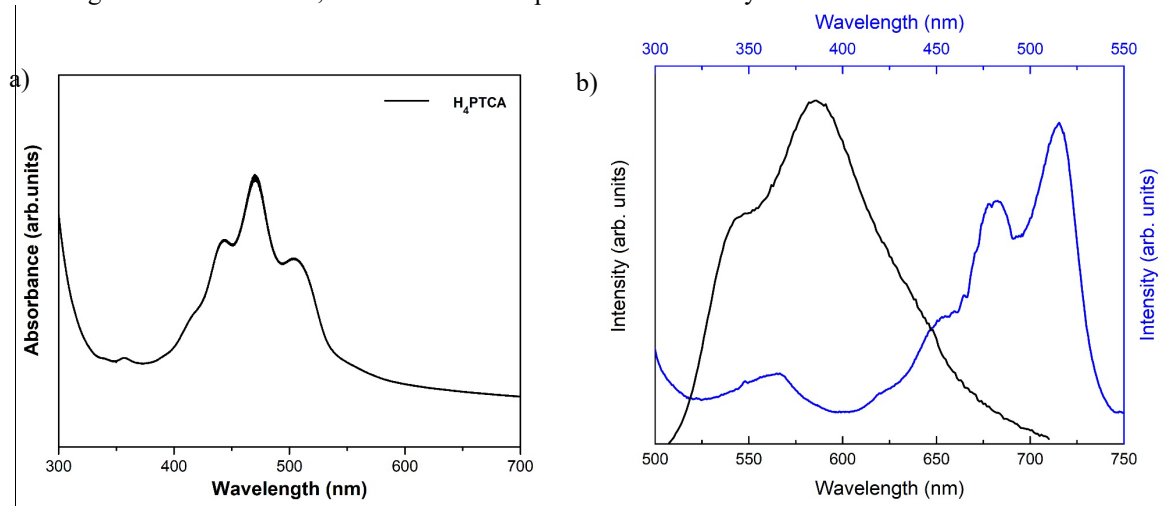

Fig. S16. a) UV/visible spectrum of the H_4PTCA ligand in DMF solution (0.05 mM). b) Excitation (blue curve) and emission (black curve) spectra of the H_4PTCA ligand in DMF solution (5 mM) monitoring at 571 nm and upon 366 nm excitation, respectively.

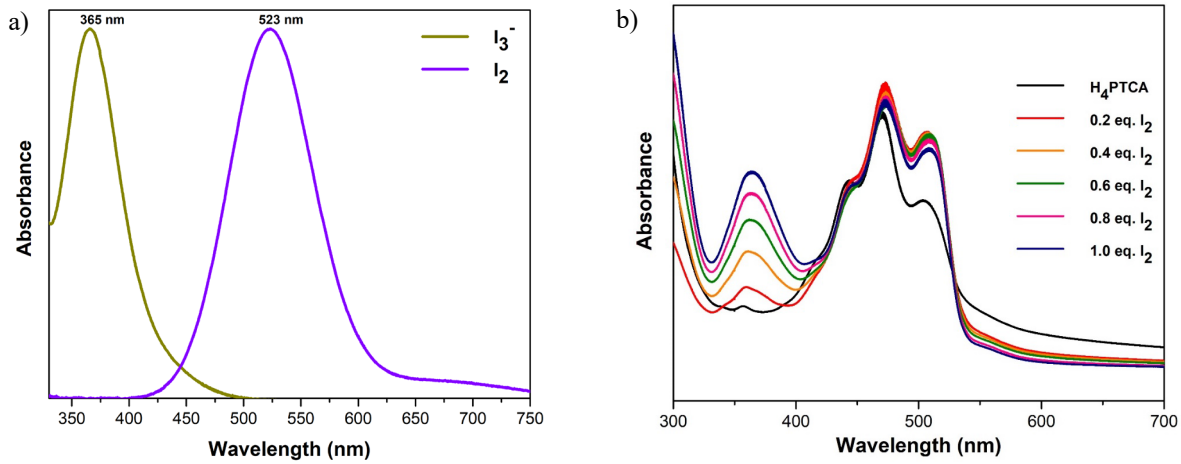

Fig. S17. UV/visible spectra of a) I_2 and I_3^- species, and b) the H_4PTCA ligand in DMF solution (0.05 mM) upon addition of increasing equivalents of I_2.

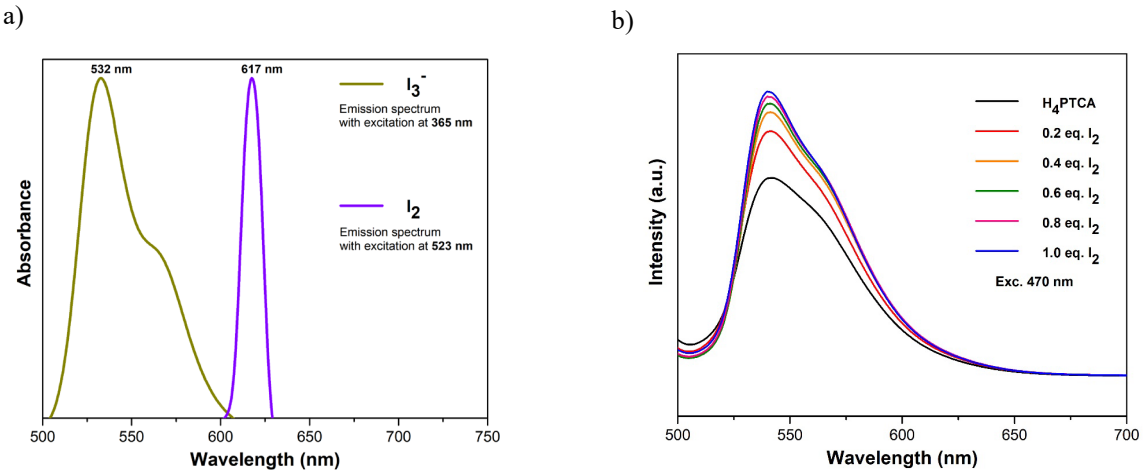

Fig. S18. Emission spectra under 470 nm excitation of a) I_2 and I_3^- species, and b) the H_4PTCA ligand in DMF solution (0.05 mM) upon addition of increasing equivalents of I_2.

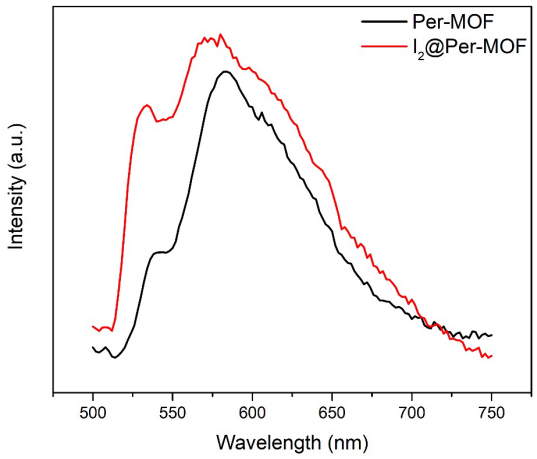

Fig. S19. Emission spectra of **Per-MOF** and **I_2@Per-MOF** under 470 nm excitation.

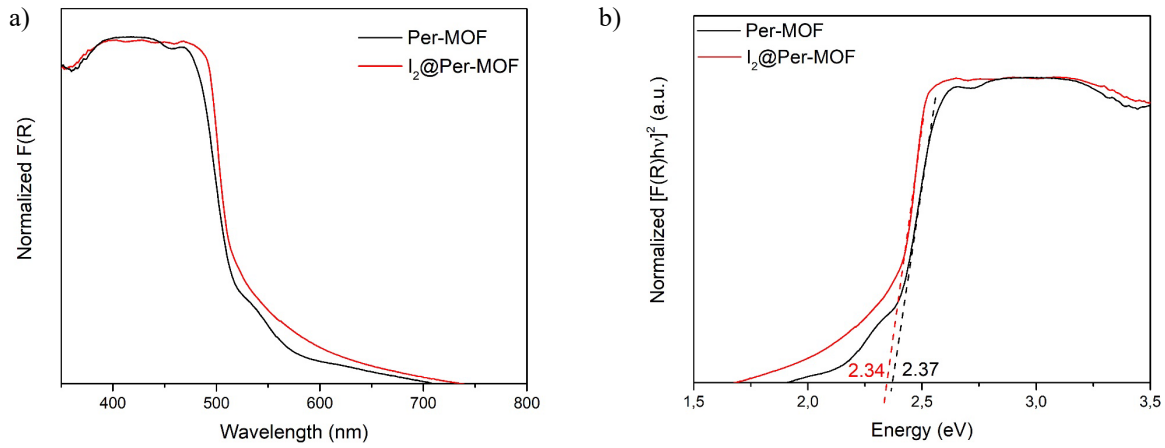

Fig. S20. a) Normalized Kubelka-Munk-transformed spectra and (b) normalized Tauc plot of the Kubelka-Munk-transformed data of **Per-MOF** and **I_2@Per-MOF**. Dashed lines indicate linear fits to the absorption onsets.

6. Quantum-chemical calculations

Molecular calculations of perylene, H_4PTCA, pyrene and pyrene 1,3,6,8-tetracarboxylic acid (H_4PyTC) in their neutral and oxidized forms and in gas phase and solvent conditions (acetonitrile) were performed under the density functional theory (DFT) framework using the Gaussian-16.A03 suite of packages.[3] First, minimum-energy structures of neutral and charged species were obtained at the PBE0/6-31G(d,p) level of theory.[4–6] Then, single-point calculations on the previously optimized geometries were performed at the HSE06/6-31G(d,p) level. Solvent effects were included using the polarized continuum model (PCM) approach as implemented in Gaussian16.A03.[7] A preliminary estimation of the ionization potential (IP) for perylene, H_4PTCA, pyrene and H_4PyTC was obtained according to the Koopman's theorem ($IP = -\varepsilon_{HOMO}$) from gas-phase calculations.[8] On the other hand, the adiabatic ionization potentials (IP) were calculated as the energy difference between the oxidized and neutral species at their corresponding minimum-energy geometries in acetonitrile.

Quantum-chemical calculations in periodic boundary conditions were performed within the density functional theory (DFT) framework as implemented in the all-electron full-potential FHI-AIMS electronic structure code package.[9–11] The minimum-energy structures of **Per-MOF**-based materials were obtained, starting from the experimental X-ray data, upon full lattice and ionic relaxation using the GGA-type PBEsol functional[12] and the numeric atom-centred orbital Tier-1 basis set. Dispersion forces were included by means of the vdW Hirshfeld correction as described by Tkatchenko and Scheffler.[13] Iodine doping was modelled by inserting one iodine molecule in the unit cell of **Per-MOF** (**[Per-MOF + I_2]**) according to the experimentally determined stoichiometry. Perylene oxidation by I_2 to form I_3^- was modelled by replacing I_2 guest for I_3 (**[Per-MOF + I_3]**) and allowing full ion and lattice relaxation. The electronic band structure, density of states (DOS) and atom-projected DOS (PDOS) were calculated using the hybrid HSE06 functional.[14] A full *k*-path in the $P\bar{3}$ first Brillouin zone of G−K−M−L−H−A−G and a 3×3×3 *k*-grid were employed. Relative PDOS was calculated for **[Per-MOF + I_2]** as the PDOS divided by the total number of atoms of each type in the unit cell.

In hopping-like models for charge transport, the rate constant of the charge transfer can be described by means of the Markus equation:[15]

$$k = \frac{2\pi}{\hbar}\frac{J^2}{\sqrt{4\pi\lambda k_b T}} e^{-\frac{(\lambda+\Delta G^\circ)^2}{4\lambda k_b T}}$$

being

$$\lambda = \lambda_1 + \lambda_2$$
$$\lambda_1 = E_N^{gC} - E_N^{gN}$$
$$\lambda_2 = E_C^{gN} - E_C^{gC}$$

where J is the electronic coupling, λ is the total reorganization energy, and $\Delta G°$ is the total change of the free energy for the electronic transfer reaction. In this case, the total reorganization energy is composed of λ_1, the reorganization energy for the neutral perylene, and λ_2, the reorganization energy for the cation form of the ligand. E_N^{gN} is the energy of the neutral perylene at its neutral geometry, E_N^{gC} is the energy of the neutral form at the cation geometry, E_C^{gN} is the energy of the cation form at the neutral geometry, and E_C^{gC} is the energy of the cation form at the cation geometry. Since the electronic couplings, in this case, are computed for the different dimers of the same molecular system (perylene), we neglect $\Delta G°$.

The electronic couplings of the different perylene dimers were computed under the fragment-orbital FO-DFT framework as implemented in FHI-AIMS, using the PBE/Tier-1 level of theory.[16] The H_{2n-1}@DA scheme was used,[17] where neutral fragment calculations are combined for hole transfer with a reset of the occupation number in the highest-occupied molecular orbital (HOMO). The reorganization energy (λ) of the perylene moiety was calculated to be 0.15 eV by means of molecular calculations at the HSE06/6-31G(d,p)[6] level. Four different calculations were performed to obtain λ: the neutral and oxidized forms at both minimum-energy geometry of the neutral and the oxidized ligand. The resulting hole-transfer rate constant obtained for **Per-MOF** by using the Markus equation and a mean value for the electronic coupling is 2.53×10^{13} s^{-1}. The electronic effect of the iodine doping on the electronic communication between perylene units was evaluated under the Time-Dependent DFT approach by modelling several perylene-guest dimers in different charged situations. The geometries were optimized at the PBE/def2-SVP level and then the lowest-lying excited states were calculated at the HSE06/def2-SVP level. A polarizable continuum solvent model was included (dielectric constant ε = 36). Figure S28 displays the lowest-lying singlet excited state calculated for perylene-I_2, [perylene]$^+$-I_2, perylene-I_3^- and [perylene]$^+$-I_3^- dimers.

Time-Dependent DFT (TD-DFT)[18–20] calculations were performed at the PBE0 level of theory for the lowest-lying excited states of H_4PTCA, radical H_4PTCA cation, I_2 and I_3^- in gas phase by using the Gaussian-16A.03 software. Vibrationally resolved absorption and emission

spectra corresponding to the low-lying transition to the bright state (S_1 for the neutral H_4PTCA, and D_9 for the radical cation of H_4PTCA) were simulated using the Franck–Condon approximation[21] as implemented in Gaussian-16A.03. The half-width-at-half-maximum (HWHM) for the vibronic Gaussian-convoluted spectra was set to 200 cm^{-1} (0.093 eV). Minimum-energy optimized geometries of the low-lying bright state were obtained, and their harmonic frequencies were calculated at the TD-DFT/PBE0/6-31G(d,p) level of theory. The excitonic coupling between perylenes in the framework was estimated in a representative dimer extracted from the minimum-energy crystal structure of **Per-MOF**, and using the electronic energy transfer (EET) analysis as implemented in Gaussian-16.A03.

The crystalline geometries, spin densities and frontier crystal orbitals were displayed using the software VESTA.[22]

Table S2. First ionization potential (IP) in eV calculated for relevant molecular systems according to the Koopman's theorem and by means of the adiabatic approach.

System	IP (Koopman's theorem)	Adiabatic IP (in ACN)
Perylene	4.84	5.04
Pyrene	5.36	5.44
H_4PTCA	5.63	5.65
H_4PyTC[a]	6.13	6.19

[a] Pyrene 1,3,6,8-tetracarboxylic acid.

Table S3. Lattice parameters and cell volume (V) calculated for the minimum-energy crystal structures of modelled MOF materials related to **Per-MOF** at the PBEsol level of theory. The experimental X-ray data are also indicated for comparison.

System	a (Å)	b (Å)	c (Å)	α (°)	β (°)	γ (°)	V (Å^3)
Per-MOF (non-evacuated)	12.05	11.96	14.03	87.8	89.7	118.2	1778.9
Per-MOF (evacuated)	11.62	11.56	13.64	90.2	90.0	120.2	1584.3
[Per-MOF + I_2]	11.62	11.73	13.63	89.9	89.0	120.8	1596.1
[Per-MOF + I_3]	11.54	11.53	13.82	90.1	89.8	120.1	1588.9
Experimental[a]	12.18	12.18	14.00	90.0	90.0	120.0	1799.9

[a] Experimental lattice parameters are calculated for the non-evacuated crystal, which contains solvent molecules within the pore.

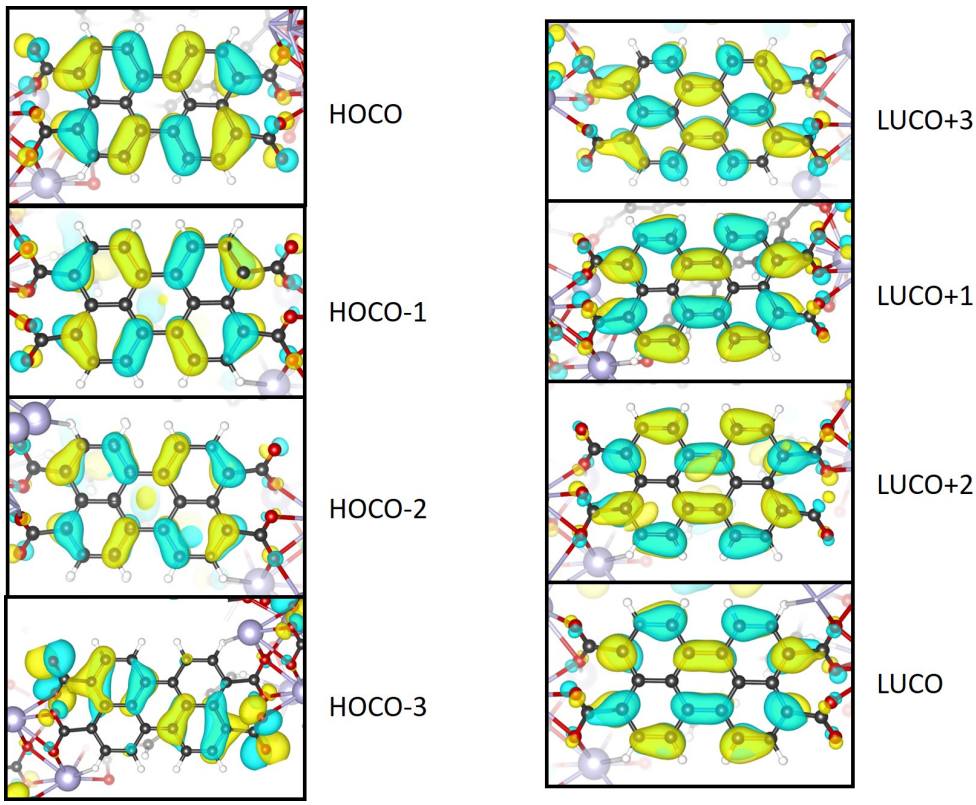

Fig. S21. Frontier crystal orbitals (isovalue contour = 0.05 au) calculated for **Per-MOF** at the HSE06 level.

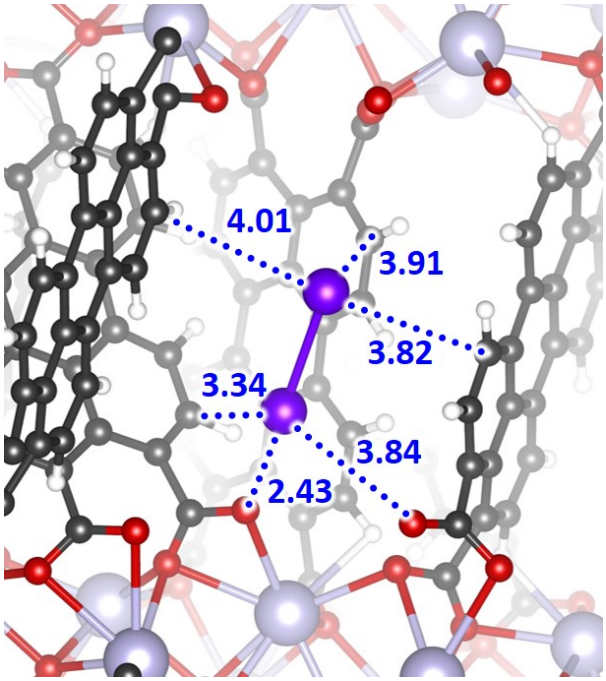

Fig. S22. Relevant intermolecular distances between iodine and the framework for the minimum-energy structure of iodine-doped **[Per-MOF + I_2]** calculated at the PBEsol level.

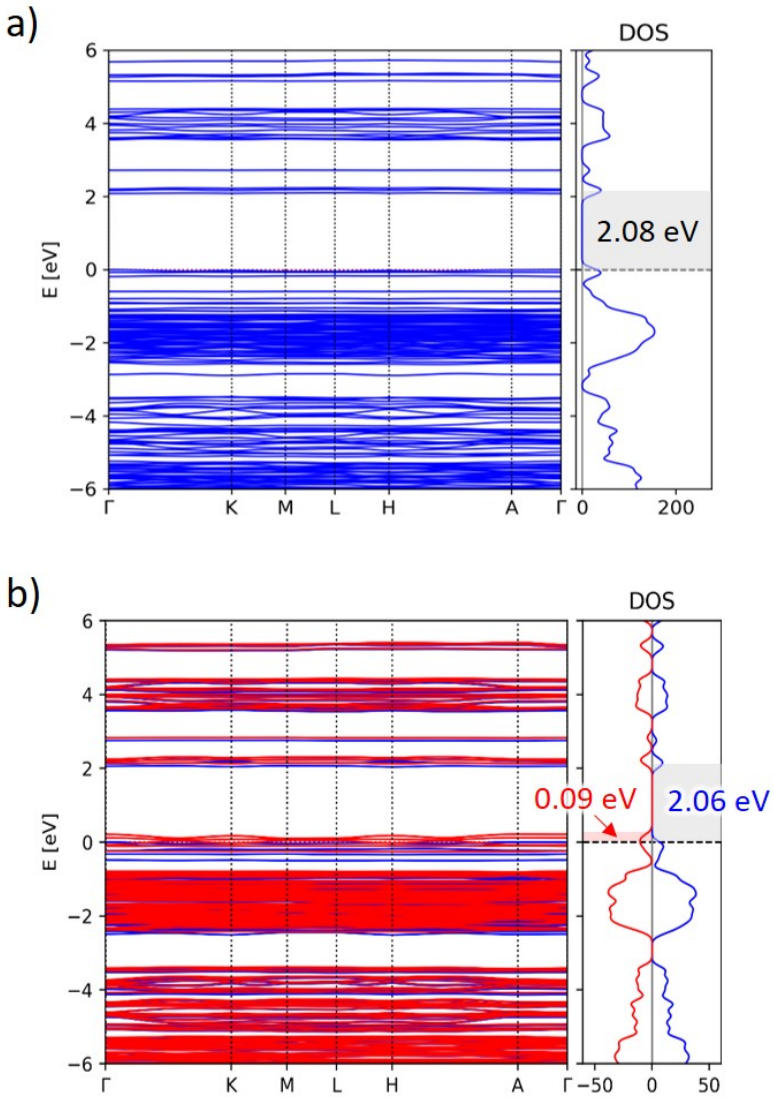

Fig. S23. Band structure and density of states (DOS) calculated at the HSE06 level for the first Brillouin zone of a) **[Per-MOF + I_2]** and b) **[Per-MOF + I_3]**.

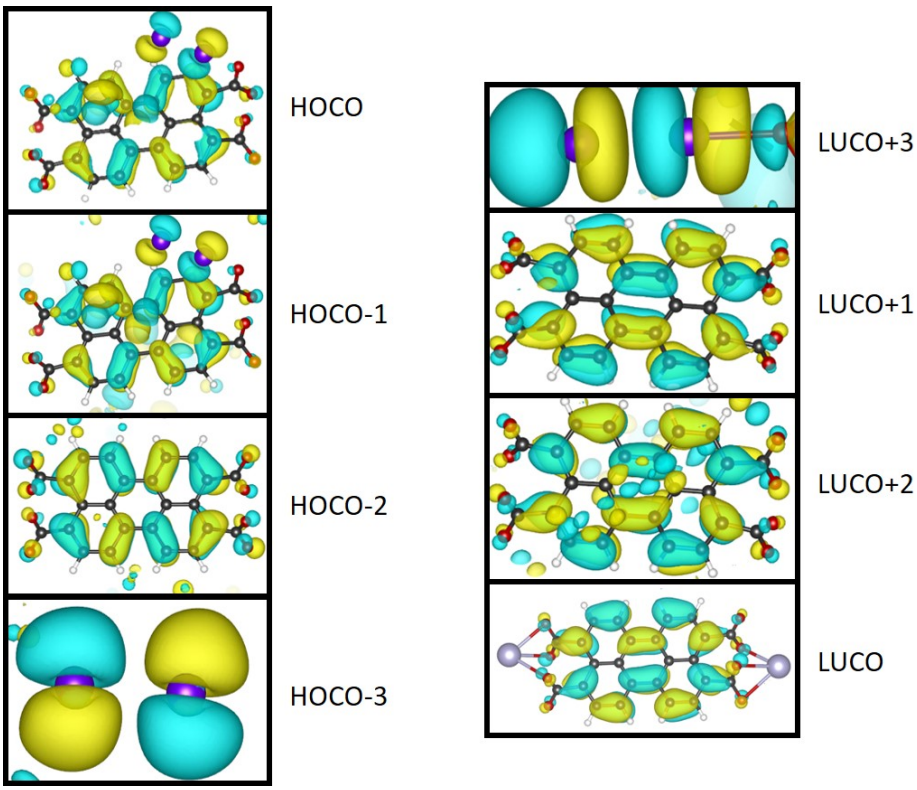

Fig. S24. Frontier crystal orbitals (isovalue contour = 0.05 au) calculated for **[Per-MOF + I_2]** at the HSE06 level.

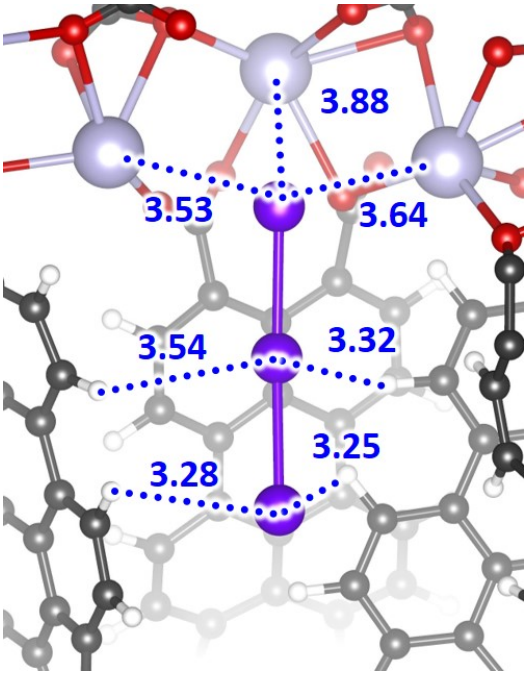

Fig. S25. Relevant intermolecular distances between triiodide and the framework for the minimum-energy structure of **[Per-MOF + I_3]** calculated at the PBEsol level.

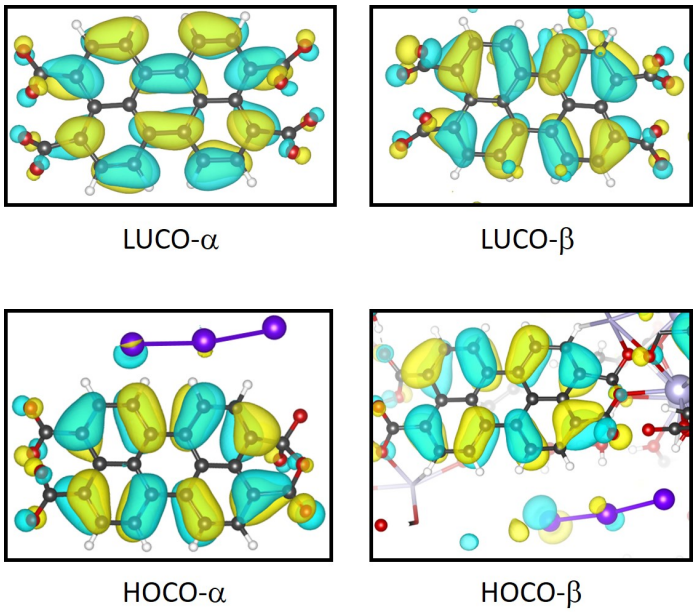

Fig. S26. Frontier crystal orbitals (isovalue contour = 0.05 au) calculated for **[Per-MOF + I_3]** at the HSE06 level.

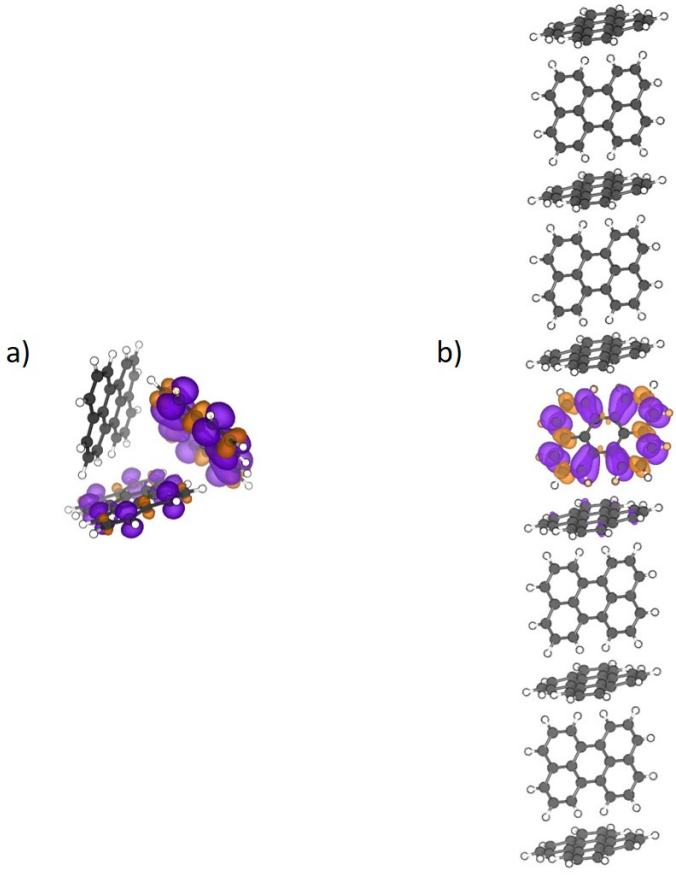

Fig. S27. Spin density contours calculated for a) trimer cluster and b) linear 11-mer, of perylene units extracted from the crystal structure of **Per-MOF**, and replacing one perylene by a fully-optimized oxidized $[perylene]^{\bullet+}$ unit. Isovalue countours were set to 0.001 au.

Table S4. Relevant parameters for quantifying the structural and electronic effects of iodine doping on the electronic communication between perylene neighbours.

MOF material	Centroid-centroid perylene intermolecular distance (Å)	Closest C–H···C intermolecular distance (Å)	J (meV)	$\bar{J}$ (meV)
Per-MOF	5.778	2.668	12.16	11.78
	5.810	2.663	11.37	
	5.781	2.651	11.82	
[Per-MOF + I_2]	5.802	2.677	7.70	11.16
	5.802	2.652	4.57	
	5.697	2.680	21.20	
[Per-MOF + I_3]	5.746	2.544	8.51	8.56
	5.749	2.537	8.61	
	5.742	2.538	8.58	

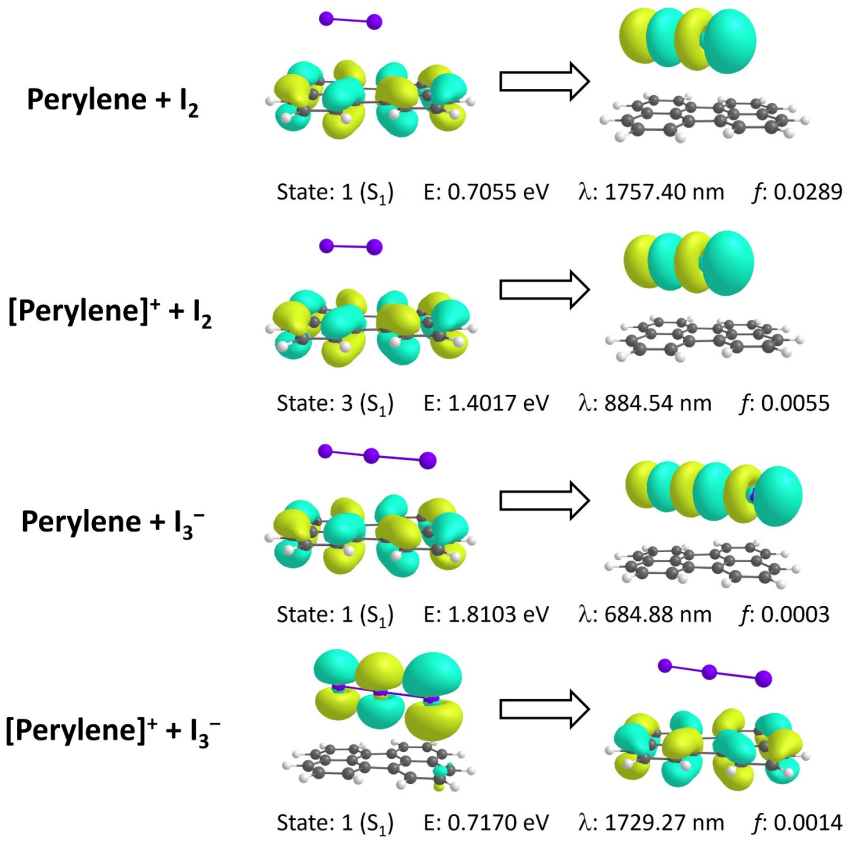

Fig. S28. Lowest-lying singlet excited states calculated for different perylene-guest neutral and charged dimers at the HSE06/def2-SVP level of theory.

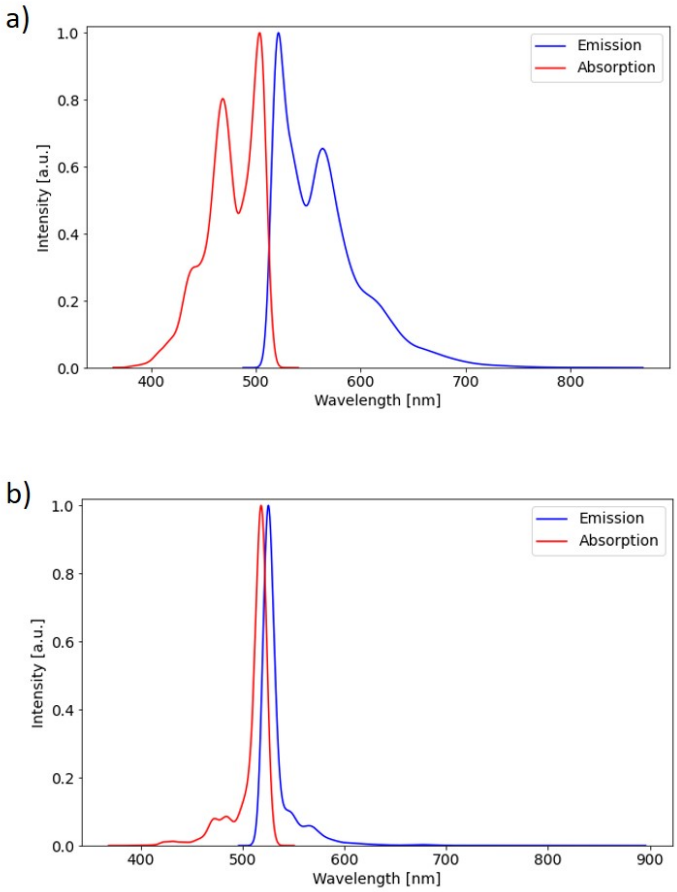

Fig. S29. Simulated absorption and emission spectra with vibrational resolution calculated at the PBE0/6-31G(d,p) level for a) H_4PTCA molecule, and b) H_4PTCA^+ radical cation. The half-width-at-half-maximum was set to 135 cm^{-1}.

Table S5. Lowest-lying singlet excited states calculated for iodine and triiodide species at the PBE0/def2-TZVP level of theory in solvent conditions (PCM with DMF as solvent). Energy of the transition (*E*), oscillator strength (*f*), and monoelectronic excitation description are indicated.

State	*E* (eV)	*E* (nm)	*f*	Monoelectronic excitation
Iodine (I_2)				
S_1	2.40	517	0.0018	H → L
S_2	2.40	517	0.0018	H-1 → L
S_3	4.17	297	0.0000	H-3 → L
S_4	4.17	297	0.0000	H-2 → L
S_5	6.87	181	0.8201	H-4 → L
Triiodide (I_3^-)				
S_1	2.71	457	0.0000	H → L
S_2	2.71	457	0.0000	H-1 → L
S_3	3.47	357	0.0024	H-3 → L
S_4	3.47	357	0.0024	H-4 → L
S_5	4.27	291	2.0166	H-2 → L

7. Electrical measurements

Per-MOF and **I_2@Per-MOF** samples were subjected to the wire-bonding process, in which a two-probe configuration was formed, with contacts that were connected to a chip-carrier by gold wires (50 μm of diameter). Two types of contacts that demonstrated similar electrical characterization results were used: silver epoxy (CircuitWorks, Ag Conductive Epoxy) and carbon-based paste (Agar Scientific, Leit-C) plus silver epoxy (Figure S31). The geometrical factors width and length were measured using an optical microscope (Motic DM-143FBGG-C + MLC-150), through the software Motic Images Plus 3.0, and the thickness was measured using a 3D Profilometer (Filmetrics, Profilm3D), through the software Profilm. *I–V* curves were obtained with a Keysight Semiconductor Device Parameter Analyzer (B1500A) and a Text Fixture (16442B), applying a voltage bias (-10 – 10 V) between the two contacts and measuring the current intensity through these contacts. The conductivity values were determined considering the samples' geometrical factors and resistance, through the equation $\sigma = \frac{1}{R} \cdot \frac{l}{w \cdot t}$ (where R is the resistance, l is the length between the contacts, and w and t are the samples' width and thickness, respectively). The values obtained for the different samples are summarized in the Table S5.

Table S6. Geometrical factors (length *l*, width *w*, and thickness *t*), resistance (*R*) obtained by the linear fit of the ohmic regime of the *I–V* curves and conductivity at 300 K for the different **Per-MOF** and **I_2@Per-MOF** samples.

Sample	*l* (μm)	*w* (μm)	*t* (μm)	*R* (Ω) at 300 K	σ (S.cm^{-1}) at 300 K
Per-MOF#1	324	300	55	$8.19 \cdot 10^{9}$	$2.40 \cdot 10^{-8}$
Per-MOF#2	239	181	55	$3.98 \cdot 10^{9}$	$6.04 \cdot 10^{-8}$
Per-MOF#3	427	234	76	$9.88 \cdot 10^{9}$	$2.43 \cdot 10^{-8}$
Per-MOF#4	451	288	81	$5.24 \cdot 10^{9}$	$3.69 \cdot 10^{-8}$
I_2@Per-MOF#1	276	224	25	$4.89 \cdot 10^{8}$	$1.00 \cdot 10^{-6}$
I_2@Per-MOF#2	180	153	58	$2.86 \cdot 10^{7}$	$7.13 \cdot 10^{-6}$
I_2@Per-MOF#3	171	132	26	$2.40 \cdot 10^{8}$	$2.05 \cdot 10^{-6}$
I_2@Per-MOF#4	186	193	85	$1.06 \cdot 10^{7}$	$1.08 \cdot 10^{-5}$
I_2@Per-MOF#5	192	154	11	$2.32 \cdot 10^{8}$	$5.01 \cdot 10^{-7}$
I_2@Per-MOF#6	237	171	12	$1.22 \cdot 10^{8}$	$9.86 \cdot 10^{-7}$
I_2@Per-MOF#7	243	138	11	$1.76 \cdot 10^{8}$	$8.68 \cdot 10^{-7}$
I_2@Per-MOF#8	311	316	11	$1.28 \cdot 10^{8}$	$7.16 \cdot 10^{-7}$
I_2@Per-MOF#9	283	284	97	$1.06 \cdot 10^{8}$	$9.71 \cdot 10^{-7}$

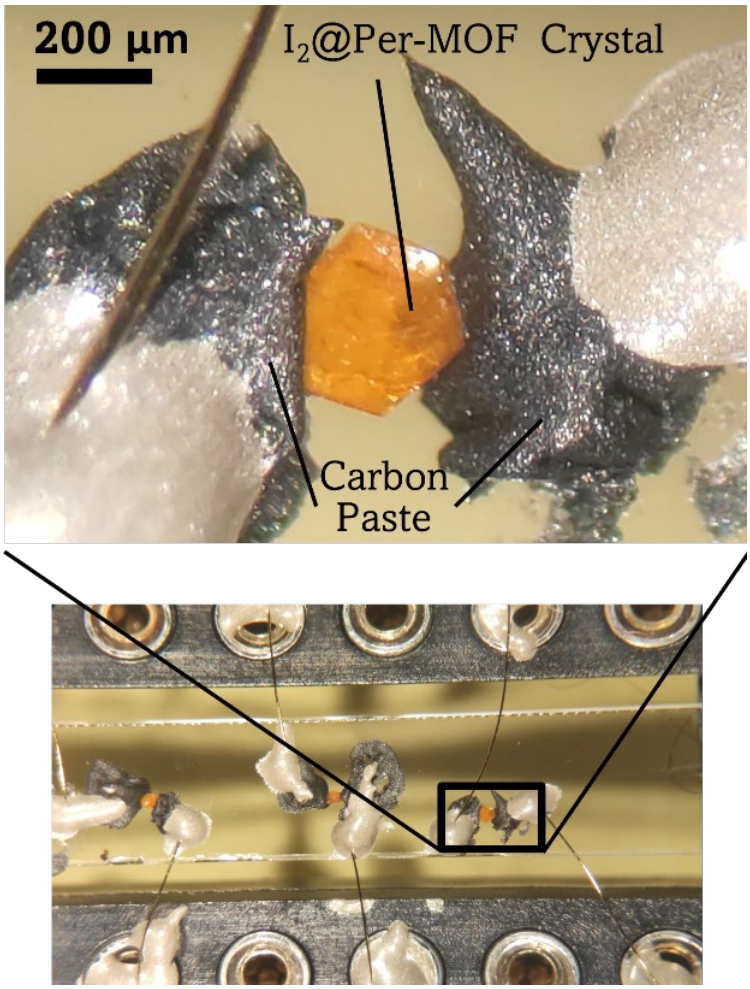

Fig. S30. Micrographs of **I_2@Per-MOF** crystal device, with carbon-based paste + silver epoxy contacts (top) and of a chip-carrier with three **I_2@Per-MOF** crystal devices (bottom).

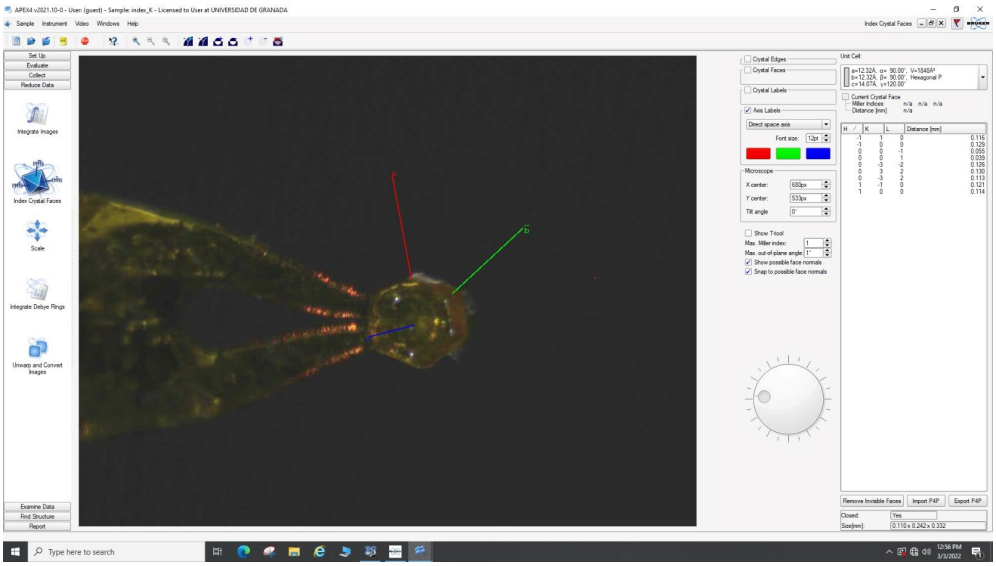

Fig. S31. Crystal indexing of **Per-MOF**.

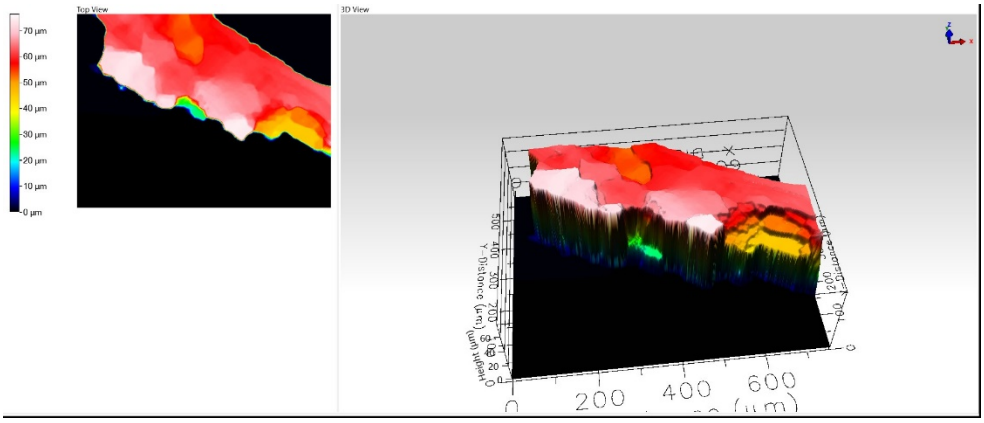

Fig. S32. Optical 3D image of **Per-MOF** crystal surface.

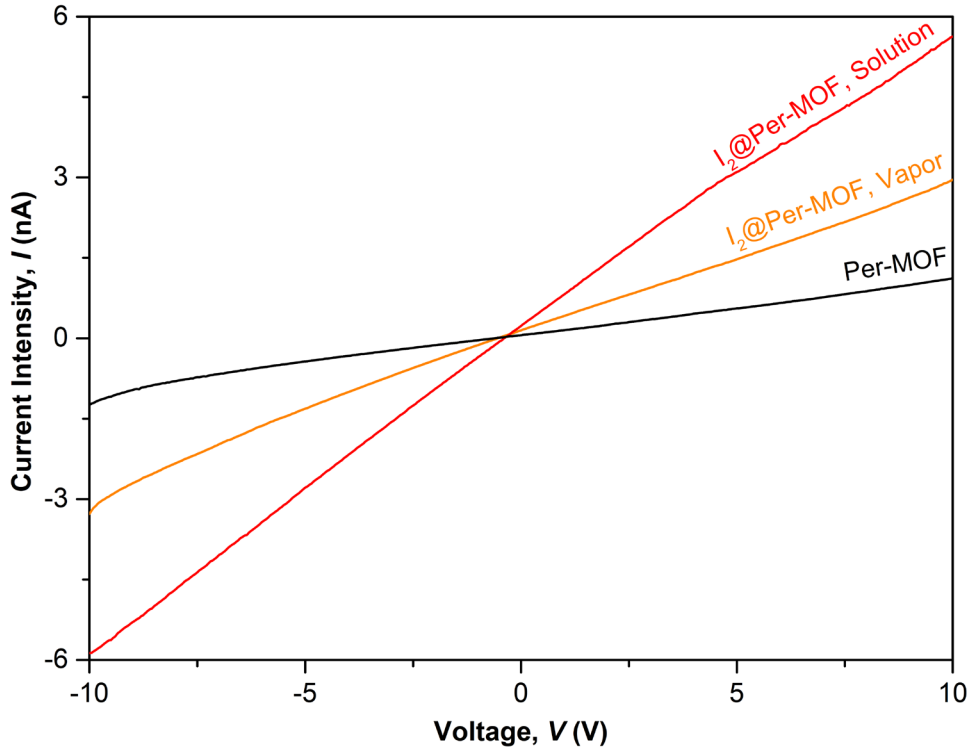

Fig. S33. Current (*I*)–Voltage (*V*) plot for crystal devices of **Per-MOF** (black), and iodine-doped **I₂@Per-MOF** through vapor doping (orange) and solution doping (red) at 300K.

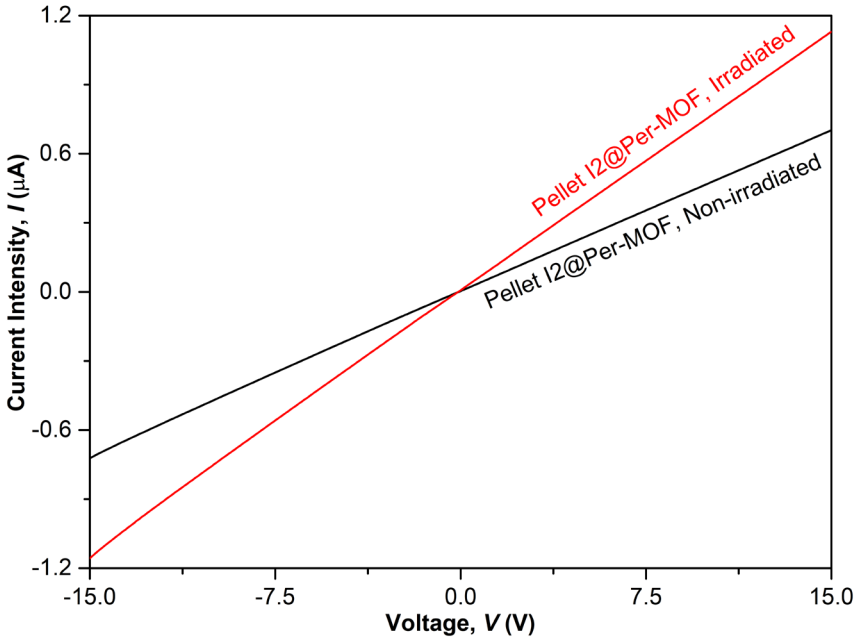

Fig. S34. Current (I)–Voltage (V) plot for pressed pellet devices of **I_2@Per-MOF** under dark (black) and white light irradiation (red) at 300 K.

8. References

(1) Seco, J. M.; San Sebastián, E.; Cepeda, J.; Biel, B.; Salinas-Castillo, A.; Fernández, B.; Morales, D. P.; Bobinger, M.; Gómez-Ruiz, S.; Loghin, F. C.; Rivadeneyra, A.; Rodríguez-Diéguez, A. A Potassium Metal-Organic Framework Based on Perylene-3,4,9,10-Tetracarboxylate as Sensing Layer for Humidity Actuators. *Sci. Rep.* **2018**, *8* (1), 1–10. https://doi.org/10.1038/s41598-018-32810-7.

(2) Dolomanov, O. V.; Bourhis, L. J.; Gildea, R. J.; Howard, J. A. K.; Puschmann, H. No Title. *J. Appl. Cryst.* **2009**, *42*, 339–341.

(3) Frisch, M. J.; Trucks, G. W.; Schlegel, H. B.; Scuseria, G. E.; Robb, M. A.; Cheeseman, J. R.; Scalmani, G.; V. Barone, G. A.; Petersson; Nakatsuji, H.; Li, X.; Caricato, M.; Marenich, A. V.; Bloino, J.; Janesko, B. G.; Gomperts, R.; Mennu, B.; Fox, D. J. Gaussian 16, Revision C. Wallingford CT 2016.

(4) Perdew, J. P.; Ernzerhof, M.; Burke, K. Rationale for Mixing Exact Exchange with Density Functional Approximations. *J. Chem. Phys.* **1996**, *105* (22), 9982–9985. https://doi.org/10.1063/1.472933.

(5) Adamo, C.; Barone, V. Toward Reliable Density Functional Methods without Adjustable Parameters: The PBE0 Model. *J. Chem. Phys.* **1999**, *110* (13), 6158–6170. https://doi.org/10.1063/1.478522.

(6) Rassolov, V. A.; Ratner, M. A.; Pople, J. A.; Redfern, P. C.; Curtiss, L. A. 6-31G* Basis Set for Third-Row Atoms. *J. Comput. Chem.* **2001**, *22* (9), 976–984. https://doi.org/10.1002/jcc.1058.

(7) Scalmani, G.; Frisch, M. J. Continuous Surface Charge Polarizable Continuum Models of Solvation. I. General Formalism. *J. Chem. Phys.* **2010**, *132* (11), 114110. https://doi.org/10.1063/1.3359469.

(8) Koopmans, T. Über Die Zuordnung von Wellenfunktionen Und Eigenwerten Zu Den Einzelnen Elektronen Eines Atoms. *Physica* **1934**, *1* (1–6), 104–113. https://doi.org/10.1016/S0031-8914(34)90011-2.

(9) Blum, V.; Gehrke, R.; Hanke, F.; Havu, P.; Havu, V.; Ren, X.; Reuter, K.; Scheffler, M. Ab Initio Molecular Simulations with Numeric Atom-Centered Orbitals. *Comput. Phys. Commun.* **2009**, *180* (11), 2175–2196. https://doi.org/10.1016/j.cpc.2009.06.022.

(10) Havu, V.; Blum, V.; Havu, P.; Scheffler, M. Efficient Integration for All-Electron Electronic Structure Calculation Using Numeric Basis Functions. *J. Comput. Phys.* **2009**, *228* (22), 8367–8379. https://doi.org/10.1016/j.jcp.2009.08.008.

(11) Ren, X.; Rinke, P.; Blum, V.; Wieferink, J.; Tkatchenko, A.; Sanfilippo, A.; Reuter, K.; Scheffler, M. Resolution-of-Identity Approach to Hartree–Fock, Hybrid Density Functionals, RPA, MP2 and GW with Numeric Atom-Centered Orbital Basis Functions. *New J. Phys.* **2012**, *14* (5), 053020. https://doi.org/10.1088/1367-2630/14/5/053020.

(12) Perdew, J. P.; Ruzsinszky, A.; Csonka, G. I.; Vydrov, O. A.; Scuseria, G. E.; Constantin, L. A.; Zhou, X.; Burke, K. Restoring the Density-Gradient Expansion for Exchange in Solids and Surfaces. *Phys. Rev. Lett.* **2008**, *100* (13), 136406. https://doi.org/10.1103/PhysRevLett.100.136406.

(13) Tkatchenko, A.; Scheffler, M. Accurate Molecular van Der Waals Interactions from Ground-State Electron Density and Free-Atom Reference Data. *Phys. Rev. Lett.* **2009**, *102* (7), 073005. https://doi.org/10.1103/PhysRevLett.102.073005.

(14) Krukau, A. V.; Vydrov, O. A.; Izmaylov, A. F.; Scuseria, G. E. Influence of the Exchange Screening Parameter on the Performance of Screened Hybrid Functionals. *J. Chem. Phys.* **2006**, *125* (22), 224106. https://doi.org/10.1063/1.2404663.

(15) Marcus, R. A. On the Theory of Oxidation-Reduction Reactions Involving Electron Transfer. I. *J. Chem. Phys.* **1956**, *24* (5), 966–978. https://doi.org/10.1063/1.1742723.

(16) Perdew, J. P.; Burke, K.; Ernzerhof, M. Generalized Gradient Approximation Made Simple. *Phys. Rev. Lett.* **1996**, *77*, 3865–3868.
(17) Senthilkumar, K.; Grozema, F. C.; Bickelhaupt, F. M.; Siebbeles, L. D. A. Charge Transport in Columnar Stacked Triphenylenes: Effects of Conformational Fluctuations on Charge Transfer Integrals and Site Energies. *J. Chem. Phys.* **2003**, *119* (18), 9809–9817. https://doi.org/10.1063/1.1615476.
(18) Jamorski, C.; Casida, M. E.; Salahub, D. R. Dynamic Polarizabilities and Excitation Spectra from a Molecular Implementation of Time-dependent Density-functional Response Theory: N 2 as a Case Study. *J. Chem. Phys.* **1996**, *104* (13), 5134–5147. https://doi.org/10.1063/1.471140.
(19) Casida, M. E.; Jamorski, C.; Casida, K. C.; Salahub, D. R. Molecular Excitation Energies to High-Lying Bound States from Time-Dependent Density-Functional Response Theory: Characterization and Correction of the Time-Dependent Local Density Approximation Ionization Threshold. *J. Chem. Phys.* **1998**, *108* (11), 4439–4449. https://doi.org/10.1063/1.475855.
(20) Petersilka, M.; Gossmann, U. J.; Gross, E. K. U. Excitation Energies from Time-Dependent Density-Functional Theory. *Phys. Rev. Lett.* **1996**, *76* (8), 1212–1215. https://doi.org/10.1103/PhysRevLett.76.1212.
(21) Franck, J.; Dymond, E. G. Elementary Processes of Photochemical Reactions. *Trans. Faraday Soc.* **1926**, *21* (February), 536. https://doi.org/10.1039/tf9262100536.
(22) Momma, K.; Izumi, F. VESTA 3 for Three-Dimensional Visualization of Crystal, Volumetric and Morphology Data. *J. Appl. Crystallogr.* **2011**, *44* (6), 1272–1276. https://doi.org/10.1107/S0021889811038970.